Formation of local and global currents in a toroidal Bose-Einstein condensate via an inhomogeneous artificial gauge field

S. Sahar S. Hejazi [1,*] Juan Polo [2] and Makoto Tsubota [1,3,4]

[1]*Department of Physics, Osaka City University, 3-3-138 Sugimoto, Osaka 558-8585, Japan*

[2]*Quantum Research Centre, Technology Innovation Institute, Abu Dhabi, United Arab Emirates*

[3]*Department of Physics and Nambu Yoichiro Institute of Theoretical and Experimental Physics (NITEP), Osaka 558-8585, Japan*

[4]*The OCU Advanced Research Institute for Natural Science and Technology (OCARINA),*
Osaka City University, 3-3-138 Sugimoto, Osaka 558-8585, Japan

We study the effects of a position-dependent artificial gauge field on an atomic Bose-Einstein condensate in quasi-one-dimensional and two-dimensional ring settings. The inhomogeneous artificial gauge field can induce global and local currents in the Bose-Einstein condensate via phase gradients along the ring and vortices, respectively. We observe two different regimes in the system depending on the radial size of the ring and the strength of the gauge field. For weak artificial gauge fields, the angular momentum increases, as expected, in a quantized manner; however, for stronger values of the fields, the angular momentum exhibits a linear (nonquantized) behavior. We also characterize the angular momentum for noncylindrically symmetric traps.

I. INTRODUCTION

Ultracold atomic gases provide excellent test beds for studying quantum phenomena in a controlled manner. They are trapped in an external potential and cooled down at their lowest-energy state [1–4]. As the temperature of the gas decreases below a critical value, a Bose-Einstein condensate (BEC) is obtained. In the mean-field approximation, a BEC trapped in an external potential is described by using a macroscopic wave function that obeys a nonlinear Schrödinger-type equation, known as the Gross-Pitaevskii equation (GPE), and has been extensively studied in various frameworks [5–8].

Cold atomic gases have been used to investigate dynamical phenomena associated with superfluidity in low temperature physics. This entails studying the formation of various vortex structures and their dynamics in a BEC [9,10] in addition to more complex nonlinear phenomena such as quantum turbulence [11–15].

Ring-shaped potentials give one of the simplest geometries that is topologically nontrivial and therefore allows persistent currents (global currents) around the whole loop. A toroidal potential can be prepared by using various methods such as painting time-dependent potentials [16] or optical lattices in the form of a ring trap with a tunable boundary phase twist, which is created by interference between the plane wave and Laguerre-Gaussian laser modes [17]. It can also be created using a radio-frequency-dressed (RF-dressed) magnetic trap with an optical potential [18], or a rapidly scanned time-averaged dipole potential [19], using a ring-shaped magnetic waveguide [20], the BEC being stored in a ring potential using a magnetic field [21]. However, in strictly one-dimensional (1D) systems vortices cannot exist and the mechanisms

inducing currents [22,23] may differ from those in two-dimensional (2D) scenarios [24,25]. Therefore, the transition between quasi-1D and 2D present substantial differences when considering nonhomogeneous artificial gauge fields.

The superfluid behavior of ultracold atomic gases, such as BECs, can also cause the appearance of topological defects, e.g., the creation of quantized vortices. In a corotating frame, superfluid vortex states correspond to a global energy minimum. Their creation process usually requires one to break the rotational symmetry at some point. For homogeneous rotations, there exists a critical rotational frequency for which vortices start to appear in a BEC [26]. This produces a sudden increase in the angular momentum and changes in the phase profile. Therefore, the appearance of vortices is triggered by a symmetry breaking, where the angular momentum is transferred into the condensate through the excitation of surface modes, resulting in the generation of vortices. The critical frequency is found to be greater than the vortex stability frequency [27]. The vortex nucleation and lattice formation in a rotating condensate has been studied theoretically [28,29] and observed experimentally [30–33].

This has led to the development of different techniques to create vortices as well as currents in BECs. For instance, stirring a BEC with a laser beam [26,30], phase imprinting [32], a rotating trap [34], a rotating laser spoon [26], rotating magnetic trap, rotating thermal cloud [35], phase engineering in two-species condensates [36], inhomogeneous synthetic magnetic fields [37], and, recently, using vector gauge potential [38–40]. The defects in BECs result in different vortex lattice structural geometries, e.g., linear vortex lattices [41] and zigzag arrangement of vortices [42]. One possible classification of vortices that allows us to distinguish different cases and phenomena is the following: (i) *visible* vortices, which can easily be detected via their density depression as well as phase winding; (ii) *hidden/invisible* vortices, which are not visible

---
*hejazi@osaka-cu.ac.jp

on the density distribution but only in the phase profile of the gas and induce a persistent current in the fluid, and (iii) *ghost* vortices that are on the outskirts of the BEC, where the density is almost negligible and carry neither angular momentum nor energy [28,43–48]. Nonetheless, such classification is purely empirical and all vortices are topologically equal.

More recently, there have been proposals with new types of artificial gauge fields [49–51] that have some position-dependent features. In such fields, the vortex structures appear at the high intensity of the effective magnetic field [38]. This position dependence of the gauge field leads to various interesting features, such as the symmetry breaking of the density profile of the two-coupled BECs [52] and also the creation of a position-dependent structure of vortices in the condensate.

In this work, we will explore the effects of an inhomogeneous gauge field on a BEC trapped in a finite-width ring geometry. This geometry is one of the simplest that is topologically nontrivial and therefore allows persistent currents (global currents) around the whole loop, while at the same time also permitting localized vortex structures.

The following is an outline of this paper. In Sec. II, we introduce our physical system and discuss how one can use light-matter interactions to create an artificial magnetic field in a BEC which is located near a dielectric prism. We present the results that correspond to a global current in a quasi-1D ring in Sec. II A. In Sec. II B, we illustrate the possibility of having visible and invisible vortices in a 2D ring trap. In Sec. III, we demonstrate how a change in the symmetry of the ring trap affects the angular momentum of the system. Finally, we conclude our observations regarding the effect of an inhomogeneous gauge field on a ring of BEC in Sec. IV.

II. LOCAL AND GLOBAL CURRENTS IN RING TRAPS

Vortices (in the bulk) and persistent currents (global currents) are two hallmarks of superfluidity, and they have recently been studied extensively in atomic BECs. While vortices are singularities within the condensate field, persistent currents are usually defined in topologically nontrivial ring settings, where they appear as a phase gradient along the azimuthal direction with the corresponding singularity located at the center of the trap where no condensate density exists.

In a simply connected condensate, the fundamental excitation is a vortex, which is defined by the appearance of a density minimum owing to a phase singularity in the condensate. In contrast, in a topologically nontrivial geometry, such as a ring trap, the fundamental excitation is a persistent current, which is a simple current along the azimuthal direction that connects onto itself after 2π.

Inducing angular momentum into a cylindrically symmetric system for instance, by rotating a harmonically trapped BEC, results in a collection of vortices with a winding number of unity, which are distributed throughout the BEC and arrange themselves in a lattice structure that is similar to the Abrikosov lattice [53–55]. This singularity in the density and the corresponding phase winding around it leads to a local current around the vortex. In contrast, considering a topologically nontrivial system, i.e., a one-dimensional ring potential, introducing the rotation leads to a persistent current along the ring, with no visible vortices. Therefore, there is a difference
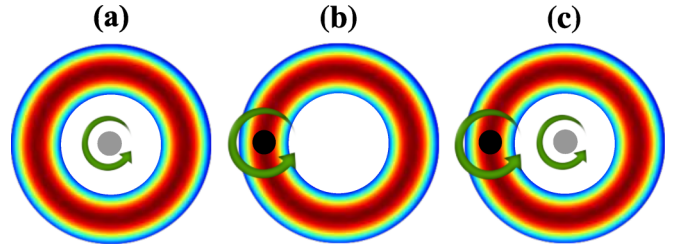

FIG. 1. Vortex configurations. Schematic of vortices in a BEC trapped in a ring potential. We consider three possible scenarios: (a) an invisible vortex (gray dot) is located at the center of the ring, and therefore the BEC experiences a global current; in plot (b) a visible vortex (black dot) results in a local current at the vicinity of where the vortex is formed; and (c) a mixture of both visible and invisible vortices. The green arrows represent an intuitive representation of the phase winding number.

in behavior between the 2D and 1D regimes. This transition can be realized, for instance, from a harmonic trap to a 2D ring and finally to a 1D ring by creating a maximum in the center of the harmonic trap and increasing its intensity, which creates a central hole [56]. There are a few methods of creating a ring trap, such as the combination of magnetic, optical, and radio-frequency fields [57], or by using time-averaged adiabatic potentials [58], and the use of a magnetic trap for RF-dressed atoms [18].

It can be naively expected that applying a localized (inhomogeneous) gauge field to the system results in local excitations around the field lines; this does occur, as shown in [52], which leads to an interesting phase separation in the immiscible regime. In this work, we demonstrate that localized magnetic fields can also induce global currents.

Two types of vortices can be formed in a ring trap that experiences an inhomogeneous artificial gauge field. The first type, herein defined as visible vortices, is located in the high-density regions of the BEC cloud, and they can be observed in the density plot as a density minima, as well as in the phase (as a phase winding around their core). The other type of vortices, also known as vortex states or current states, we define as invisible vortices which form in the central part of the trap and can just be detected via phase measurements, e.g., by measuring the particle current [see Fig. 1(a)].

As vortices have an associated angular momentum around their core, they induce rotation into the BEC cloud, and the presence of visible and invisible vortices results in three different situations: (a) if the invisible vortex is at the center of the BEC ring, it induces a global current as it acts as the BEC is rotating with an external source; (b) when the vortex is in the high-density regions of the BEC forming a density dip, it creates a local current in the BEC; and (c) a mixture of two types of vortices creates a mixture of global and local currents (See a schematic of these vortex configurations in Fig. 1).

III. MODEL AND HAMILTONIAN

We consider a BEC of neutral alkali-metal atoms trapped in a ring potential along the *x*-*z* plane in the vicinity of a dielectric prism (see Fig. 2). The BEC is tightly confined along the other spatial direction *y*, such that it can be effectively treated
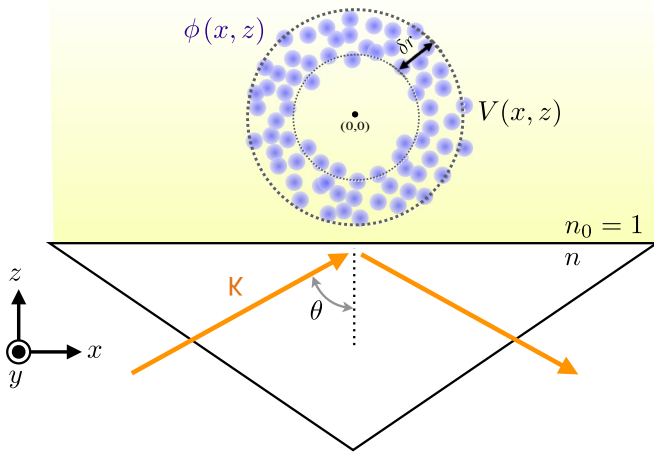
FIG. 2. Schematic of a BEC cloud with wave function $\phi(x,z)$ trapped in an external ring potential $V(x,z)$, with thickness δr for the ring BEC. The cold gas is located in the vicinity of a dielectric prism having a reflective index of n. The orange line indicates the input laser field with wave vector **k** and the incident angle θ.

as a two-dimensional system [5]. The ring potential has the form $V(x,z) = \frac{1}{2}m(\sqrt{\omega_x^2 x^2 + \omega_z^2 z^2} - r_0)^2$, with the frequencies of ω_x and ω_z in the x and z directions, respectively; m is the mass of the atomic BEC, and r_0 corresponds to the inner radius of the ring. This ring trap is in the vacuum ($n_0 = 1$) just above the surface of a dielectric prism having a refractive index n. We choose our Cartesian coordinate system in such a way that the center of the ring potential is located at the origin $(0,0)$ of the coordinate system, and the upward direction is considered as positive.

For the circular ring trap, we consider $\omega_x = \omega_z$; however, in the elliptical case we consider $\omega_x \neq \omega_z$. The BEC is created from ultracold alkali-metal atoms, and each atom has two internal states: the ground state $|g\rangle$ and the excited state $|e\rangle$.

The incident laser beam has the wave vector **k** and frequency ω_L, which is selected to be close to the resonance frequency of the atomic transition, and propagates inside of the prism under an angle, θ, with respect to the interface of the prism under vacuum. The propagation angle, θ, is selected in such a way that the beam undergoes total internal reflection, i.e., it is greater than the critical angle, $\theta_0 = \arcsin(1/n)$, which leads to the creation of an evanescent field at the surface of the prism. The electromagnetic field, $\mathbf{E}(x,z,t)$, propagates in the x-z plane with an amplitude $\mathbf{E}_0$ and decays at the surface in the positive z direction with a penetration depth d. This can be written as $\mathbf{E}(x,z,t) = t^{\text{TE}}(\theta)\mathbf{E}_0 e^{-i[\omega t - \Phi(x)]}e^{-z/d}$, with t^{TE} as the transmission coefficient, and the running phase $\Phi(x)$ as shown in [38].

The interaction between the evanescent field and the atoms in the condensate occurs via a dipole coupling, $\mathbf{d} \cdot \mathbf{E}(x,z)$, where **d** is the electric dipole moment of the atoms. For simplicity, we assume that both types of atoms have the same dipole moment and consider the rotating wave approximation for the dressed states of the atom when they interact with the light field. From this dressed state, the vector potential can be
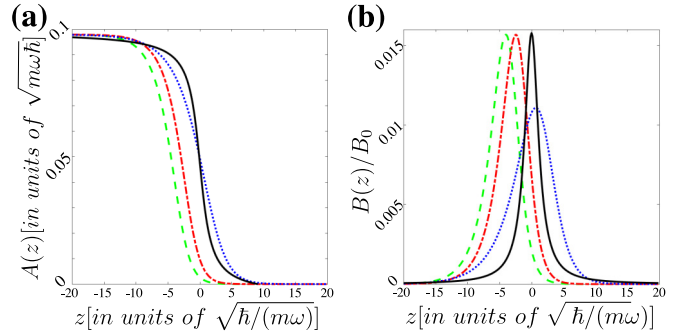

FIG. 3. (a) Artificial gauge field and (b) normalized magnetic field $B(z)/B_0$ is plotted as a function of the position z. The prism is located at $z = -20$. The green dashed (– – – –) and red dot-dashed (– · – · – ·) lines correspond to an incident angle of $\theta - \theta_0 = 8 \times 10^{-4}$ rad and $s = 10$ and $s = 20$, respectively. The blue dotted (·········) curve corresponds to $\theta - \theta_0 = 4 \times 10^{-4}$ rad for $s = 20$. The black line corresponds to our toy model $A_{\text{Model}}(z) = -0.1[\arctan(\frac{z}{\beta}) - \frac{\pi}{2}]/\pi$, where $\beta = 1.3$.

calculated as follows [38]:

$$\mathbf{A}(x,z) = \frac{n\hbar k_0}{2}\left[1 - \frac{1}{\sqrt{1 + \left|\frac{\kappa(x,z)}{\Delta}\right|^2}}\right]\sin\theta \,\hat{\mathbf{x}}, \quad (1)$$

where k_0 is the amplitude of the wave vector **k**, $\Delta = \omega_L - \omega$ is the detuning of the laser light from the atomic resonance frequency, and the parameter $\kappa(x,z) = \mathbf{d} \cdot \mathbf{E}(x,z)/\hbar$ indicates the coupling between the electric field of the evanescent field and the dipole of atoms. The magnetic field can be calculated from the vector potential as $\mathbf{B} = \nabla \times \mathbf{A}$ [38]. Hereafter, we work in the harmonic oscillator unit as $x \to x/a_0$, $z \to z/a_0$, and $t \to t\omega$, with $a_0 = \sqrt{\hbar/m\omega}$.

A system that consists of a BEC cloud in the presence of the evanescent field can be described via the mean-field approach with the GPE as

$$i\frac{\partial\phi}{\partial t} = \left[-\frac{1}{2}(\nabla + i\mathbf{A})^2 + V_{\text{eff}} + g|\phi|^2\right]\phi, \quad (2)$$

where ϕ is the wave function of the BEC in the mean-field description and g is the coupling coefficient. In the above equation, all the parameters are scaled in harmonic oscillator units [59]. Here, we consider that the effective V_{eff} creates a trap potential in the form of a ring.

In Fig. 3, we plot the artificial gauge field A and magnetic field $B(z)$ versus the position z for various detunings and also two different incident angles. For simplicity, we consider that the artificial gauge field of our model has the form

$$\mathbf{A}_{\text{Model}}(z) = -w_0\left[\arctan\left(\frac{z}{\beta}\right) - \frac{\pi}{2}\right]\hat{\mathbf{x}}, \quad (3)$$

where w_0 modulates the amplitude, and β is the steepness of the magnetic field ($\beta \neq 0$). This results in the magnetic field $|B_{\text{Model}}(x,z)| = (\beta w_0)/(z^2 + \beta^2)$. The field presented in Eq. (1) reduces the number of parameters present in the experimentally realistic artificial gauge field while retaining its main features. The two parameters, β and w_0, can be used to change the steepness as well as the amplitude.

To understand how this inhomogeneous artificial gauge field affects the BEC trapped in the ring potential, we introduce the artificial gauge field $A_{\mathrm{Model}}(z)$ from Eq. (3) into the GPE, from Eq. (2), and solve the resulting equation numerically.

We compare the thickness of the BEC with the healing length to define two regimes for which the quasi-one- and two-dimensional ring is able to sustain vortices or not. The healing length is calculated by comparing the interaction energy (ng) with the kinetic energy ($n = |\psi|^2$) and considering a fixed value for a given system [60]. We also consider $|\mathbf{A}_{\mathrm{Model}}(x, z)| = A(x, z)$ henceforth in the paper. However, for a system that experiences an inhomogeneous artificial gauge field, the spatial scale can be written as $\xi_A = \frac{\hbar}{A(x,z)+\sqrt{2ng}}$ (see Appendix C for details). As the artificial gauge field is not constant, the healing length is modified as the strength of the gauge field changes. For this calculation, we take the maximum of the A field. In the limiting case where the strength of the gauge field is zero, i.e., $w_0 = 0$, the spatial scale leads to the well-known equation $\xi_0 = \hbar/\sqrt{2ng}$, and for a strong artificial gauge field the spatial scale of the healing length is reduced. This means that vortices created by an inhomogeneous artificial gauge field will have a smaller vortex-core size as compared to homogeneous artificial gauge fields, as the typical length scale of the vortices is proportional to the local healing length of the system. Therefore, there exists a competition between the size of the ring, which is fixed for a given system, and the healing length ξ_A. The value of n for a trapped BEC is replaced by the maximum of density $\bar{n}$, namely, $n \approx \bar{n}$. By numerical inspection, we find that vortices start to appear whenever $\delta r \gtrsim 16\sqrt{2}\xi_A$, with δr being the thickness of the ring. The typical length scale of the vortex core in a BEC is given by $\sqrt{2}\xi_A$. However, this does not give the true size of the vortex core, which will also depend on the trapping and gauge field applied. Therefore, this threshold gives an approximate phenomenological value for which vortices appear in the bulk (more details in Appendix D).

In the following, we study the current induced by an inhomogeneous artificial magnetic field that changes along z in the form of an arctangent [see Eq. (3)]. Herein, we address how the angular momentum of this system changes as the ring transitions from a one-dimensional ring, namely, a ring of BEC with negligible thickness, into a two-dimensional ring, i.e., a ring of BEC with substantial thickness. This has been used to study the role of dimensionality and has also been explored experimentally [61]. We also study how tilting the trapping potential and adding a small asymmetry can result in a different behavior of the angular momentum. In this work, we mainly focus on artificial gauge fields with large gradients and vary the amplitude (see Fig. 3) as it will highlight the inhomogeneous effects of the artificial gauge field.

A. Global currents in quasi-1D ring

In this section, we present the results obtained from a BEC in a narrow ring potential. The parameters of the ring trap have been selected such that the BEC in the trap can be considered a quasi-one-dimensional BEC.

The number of vortices is strongly related to the strength of the artificial gauge field. In particular, by increasing the strength of the magnetic field, invisible vortices appear in the
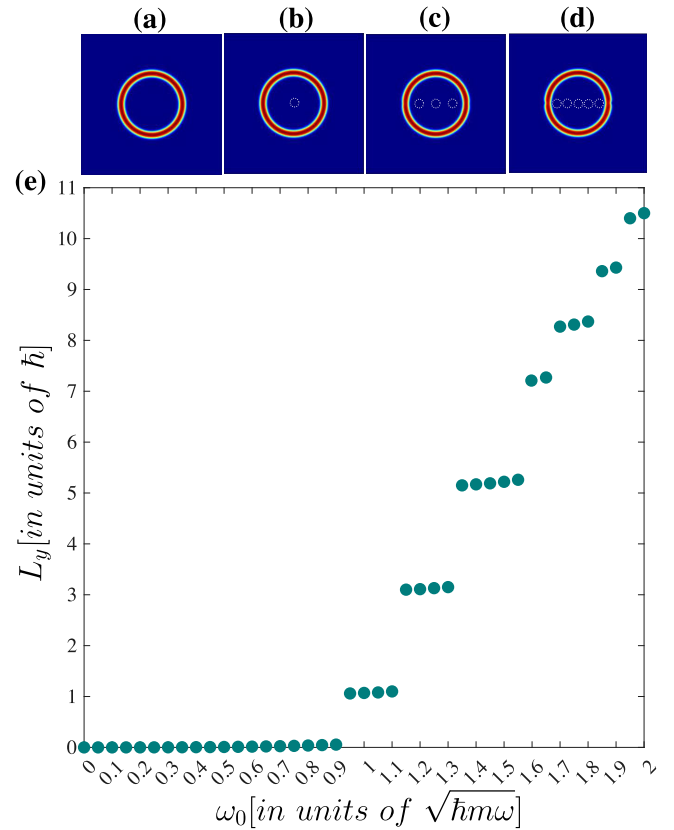

FIG. 4. Quantized regime for a quasi-1D ring. The angular momentum L_y of a narrow ring of the BEC is plotted with respect to the strength of the artificial gauge field w_0. The density plot of the BEC is shown with the location of invisible vortices for (a) $w_0 = 0$, (b) $w_0 = 1.00$, (c) $w_0 = 1.20$, and (d) $w_0 = 1.35$ with $\beta = \frac{1}{8}$. The trapping potential has $r_0 = 6.5$ and $v_0 = 5.66$. All parameters are given in harmonic oscillator units.

central region of the trapped BEC, inducing an angular momentum in a quantized manner. This can be observed through the phase as a linearly increasing function from 0 to multiples of 2π in the azimuthal direction.

In Fig. 4 (top row), we present the density of a ring of BEC for various values of strengths of the artificial gauge field (a) $w_0 = 0$, (b) $w_0 = 1.00$, (c) $w_0 = 1.20$, and (d) $w_0 = 1.35$ for the BEC with the coupling coefficient of $g = 800$. We consider a ring trap which has the potential $V_{\mathrm{circular}} = \frac{1}{2}v_0^2(\sqrt{x^2 + z^2} - r_0)^2$. Figure 4(e) displays the angular momentum, $L_y = (\mathbf{r} \times \mathbf{p})_y = -i\hbar(z\partial_x - x\partial_z)$, versus the strength of the artificial gauge field w_0. Panel (a), where $w_0 = 0$, does not have any artificial gauge field, therefore presenting no current in the ring. For a higher value of w_0, although the density plot does not change significantly, the presence of the invisible vortices results in a change in the global current. Here we show the location of the invisible vortices with dotted circles. In panel (b), where $w_0 = 1.00$, there exists just one invisible vortex, which results in a global current with one unit of angular momentum and azimuthal phase gradient of 2π. Due to the single-axis dependence of the artificial gauge field, z, and the symmetry of the trapping potential, as the strength of the gauge field increases, the number of invisible
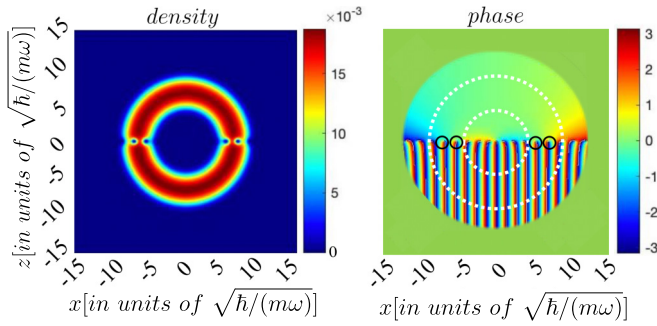
FIG. 5. Visible and invisible vortices. The density (left figure) and phase (right figure) of the BEC trapped in a ring potential of parameters $v_0 = 1.34$, and radius of $r_0 = 6.5$. The strength of the gauge field is $w_0 = 1.5$ with $\beta = 1/8$. The white dashes in the phase plot show the position of the trap, and the black circles indicate the locations of visible vortices.

vortices does not always occur in steps of one. To address this symmetry effect, we consider elliptical ring traps with certain tiltings (see Sec IV). For example, at $w_0 = 1.20$ in panel (c), we see that two invisible vortices come from left and right into the system, as well as three invisible vortices which can be detected from the phase plot with 6π. Finally, we note that, as discussed above, for large values of ω_0 the healing length will be largely reduced and it is expected that vortices will start to appear even for thin rings (which still retain some 2D character).

B. Visible and invisible vortices in quasi-2D rings

In this section, we consider a wider potential (a ring potential with thicker radius). As the thickness of the ring of the BEC, δr_{ring}, is substantial as compared to the healing length ξ, the trap can hold visible vortices in it. As shown in Fig. 5, at a high value of the gauge field, for example $w_0 = 1.50$, visible vortices appear in the BEC, in addition to invisible vortices in the low density. The presence of the invisible vortices here is the result of the inhomogeneous gauge field, which is related to the phase plot. Note, however, that the presence of the artificial gauge field redefines the probability current as discussed in Appendix C.

In this regime of the trap thickness, two different types of behavior of the angular momentum are observed: quantized and linear regimes, as shown in Fig. 6. When increasing the strength of the artificial gauge field, the system first presents invisible vortices. However, on further increasing the artificial gauge field, visible vortices start to appear in the high-density regions of the BEC (see Fig. 6, at $w_0 = 0.8$). For example, in Fig. 6(c), there are five invisible vortices that can be found through the phase profile of the BEC (as shown in Fig. 5). Moreover, as the the strength of the gauge field increases, the angular momentum L_y starts to increase linearly with respect to the strength of the gauge field (see Fig. 6). It should be noted that the same symmetry argument, discussed at the end of the previous sections, can also be made here regarding the increase in the two units of angular momentum.

This transition from a quantized angular momentum to a linear regime can also be observed in harmonically trapped
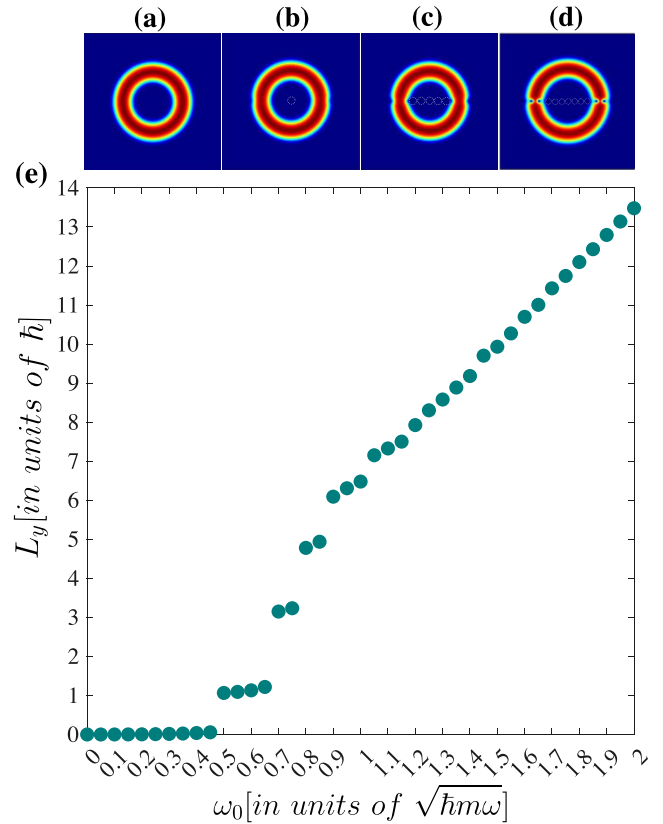

FIG. 6. Quantized and linear regimes of a 2D ring. Density plot of the BEC ground state in a ring of radius $r_0 = 6.5$ that has a gauge field strength of (a) $w_0 = 0$, (b) $w_0 = 0.50$, (c) $w_0 = 0.80$, and (d) $w_0 = 1.50$ with $\beta = 1/8$ and $v_0 = 1.34$. Panel (a) shows the density of the ground state of the cloud of the BEC when there is no artificial gauge field. As the strength of the gauge field increases, at first the invisible vortices enter the system, as can be observed in panel (b), and the angular momentum increases by quanta of one. In panel (c), there are five invisible vortices in the BEC which lead to a 10π phase. Finally, in panel (d), visible vortices enter the BEC and the angular momentum is 20π. (e) presents the angular momentum of L_y with respect to the strength of the artificial gauge field w_0. This plot shows both quantized and linear regimes of the angular momentum. For comparison, please refer to the angular momentum plot of the harmonic trap in Fig. 8, as it exhibits the same behavior.

BECs (see Fig. 8 in the Appendix). This effect originates in the inhomogeneity of the artificial gauge field rather than the geometry of the trapping potential. In the case of ring traps, we estimate that this linear behavior starts to appear whenever the thickness of the ring of BEC, δr, is comparable with the healing length, ξ_A. Therefore, vortices start to appear in the bulk, and the healing length is substantially affected by the artificial gauge field. In the harmonic trap, however, vortices start to appear at smaller values of w_0 (see Appendix A) in the high-density region (center of the trap), and thus, the linearization of L_y also occurs sooner. In our simulation, the maximum density of the ground state for the harmonic trap considered in Appendix A is $\bar{n} = 4.4 \times 10^{-3}$, in natural units ($\hbar = m = 1$) with interaction strength of $g = 800$; in the case
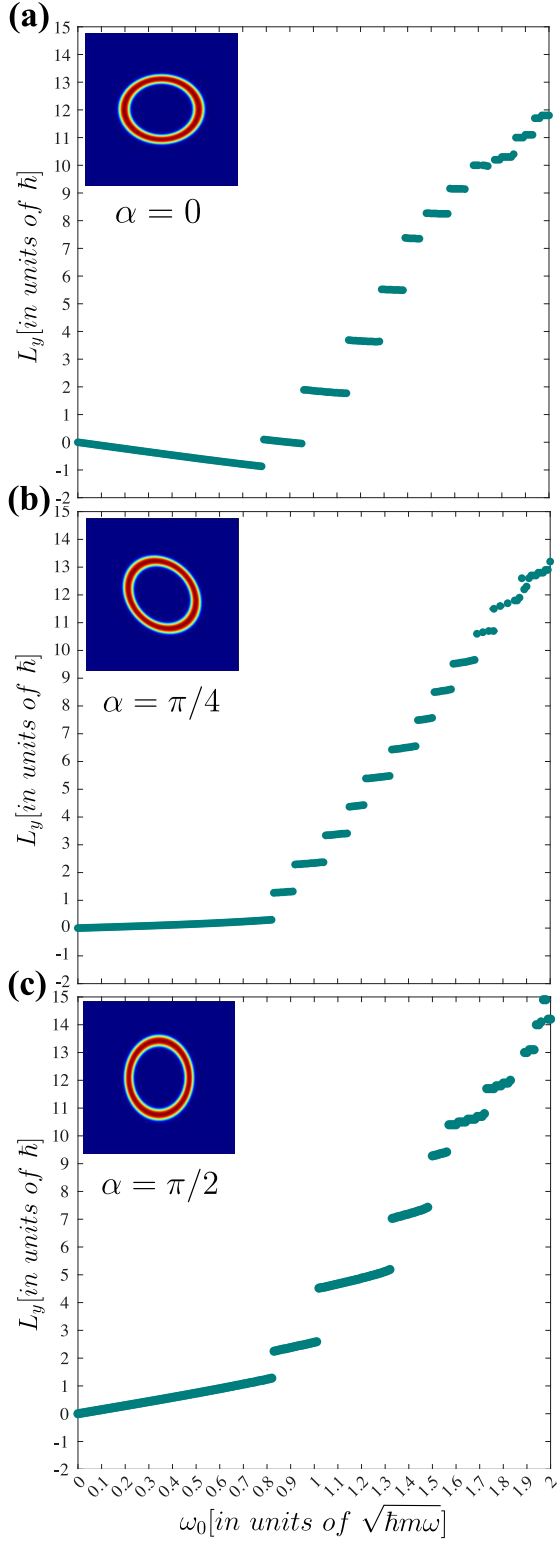
FIG. 7. Symmetry breaking of angular momentum. We plot the angular momentum of an elliptical ring versus ω_0, as shown in Eq. (4) with $\eta = 0.9$, $r_0 = 6.5$, $\gamma = \pi/2$, and $v_0 = 4$. The elliptical ring has semiminor and semimajor axes of $(1,1.5)$, plotted for various angles: (a) $\alpha = 0$, (b) $\alpha = \pi/4$, and (c) $\alpha = \pi/2$. All parameters are given in harmonic oscillator units.
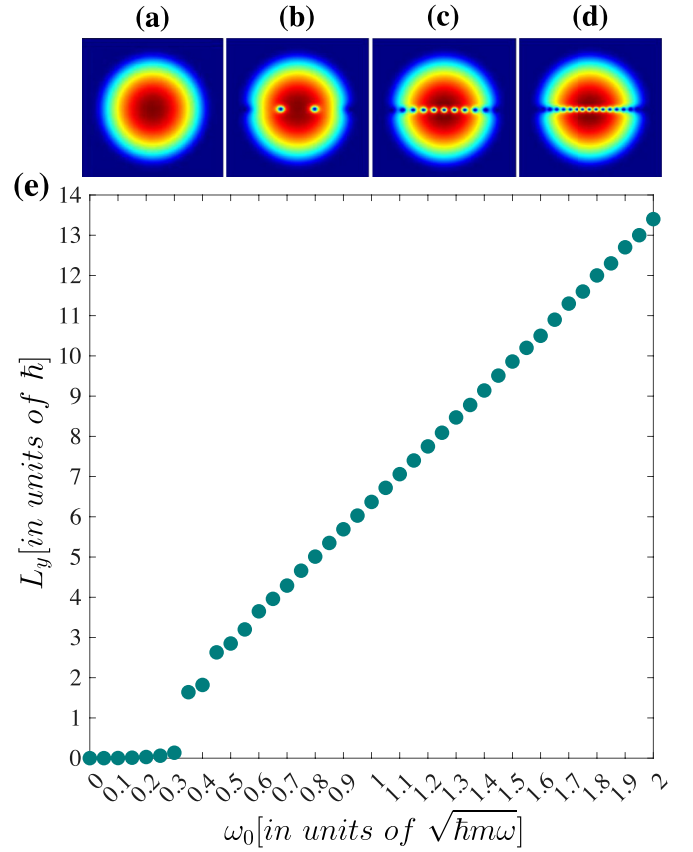

FIG. 8. Harmonic oscillator. Panels (a)–(d) show the density plot of a BEC trapped in a harmonic potential $V_{\text{harmonic}} = \frac{1}{2}v_0^2(x^2 + z^2)$. The artificial gauge field has the same value as Fig. 6 with $v_0 = 0.22$. The strength of the gauge field is (a) $w_0 = 0$, (b) $w_0 = 0.40$, (c) $w_0 = 1.00$, and (d) $w_0 = 1.50$. In plot (e) the angular momentum L_y is plotted with respect to the gauge field strength, w_0. All parameters are given in harmonic oscillator units.

of the ring trap, we have $\bar{n} = 7.9 \times 10^{-3}$, and consequently, $\xi_{0,\text{ring}} \approx 0.28$.

IV. SYMMETRY BREAKING IN THE ELLIPTICAL RING TRAP

We have mentioned in Sec. III B that the system is highly sensitive to the symmetries of the ring and artificial gauge field. Therefore, in this section we analyze how a small asymmetry in the trapping potential can affect measurable quantities such as the angular momentum. Instead of considering a perfect circular ring, we consider a more realistic situation with a slightly deformed elliptical ring.

In particular, we look at the response of the angular momentum to different tilting angles of the major axis of an elliptical trap and compare it with the circular case. Moreover, for completeness, we also compare this with a homogeneous gauge field that represents a global rotation in Appendix C.

For an ellipse with a semimajor axis a and semiminor axis b, the equation is given by $x^2/a^2 + z^2/b^2 = 1$, where the

eccentricity of the ellipse is $e = \sqrt{1 - a^2/b^2}$. By changing the eccentricity e of the ring trap from a circle with $e = 1$ to an elliptical trap with $e < 1$ and then tilting the major axis, one can observe that the angular momentum of the system changes as the tilting changes. In order to take into consideration the tilting of the ellipse with respect to the x coordinate, we replace x by $x \cos \gamma$ and y by $y \sin \gamma$, and the potential thus becomes

$$V_{\text{elliptical}}(x, z) = \frac{v_0^2}{2} \left(\eta \sqrt{\frac{x^2}{a^2} \cos^2 \gamma + \frac{z^2}{b^2} \sin^2 \gamma} - r_0^2 \right). \quad (4)$$

Figure 7 shows that the angular momentum of a BEC confined in a tight elliptical trap is considerably affected by the change in the axial trap with respect to the high-density line of the magnetic field. In each figure, the angular momentum of the elliptical ring BEC with eccentricity $e = 0.745$ ($a = 1$, $b = 1.5$) is plotted for (a) the tilting angle $\alpha = 0$, (b) $\alpha = \pi/4$, and (c) $\alpha = \pi/2$ with $\eta = 0.9$, $r_0 = 6.5$, and $\gamma = \pi/2$. We show that, for elliptical traps, the angular momentum does not present flattop steps, but has a linear dependence on the artificial magnetic field with a slope that depends on the tilting angle of the ellipse α. (See Figure 4 for comparison, as the angular momentum in the quantized regime increases by an integer number.)

In this figure, we observe that the angular momentum does not always increase in a quantized manner. It also does not increase linearly with respect to the increase in the strength of the artificial gauge field, in which it depends on ellipticity and the angle of tilting of the trapping potential with respect to inhomogeneous artificial gauge field (Fig. 8).

For instance, as shown in Fig. 7(a), the angular momentum steps of the elliptical trap with a tilting angle of $\alpha = 0$, in comparison with the circular flat steps, decreases linearly as the strength of the artificial gauge field increases. However, for $\alpha = \pi/2$, the situation is opposite, as w_0 increases the "plateaus" displayed by the angular moment increase linearly again. All this occurs while the angular momentum presents quantizedlike jumps of total angular momentum L_y. We also note that, for a tilting angle of $\alpha = \pi/4$, the angular moment of the elliptical ring of the BEC exhibits the same behavior as that observed for the circular potential with almost flat plateaus.

Quite interestingly, such behavior is not observed in the case of homogeneous artificial gauge fields such as rotations (see Appendix A). Owing to the quantized circulation of superfluids and the continuity of the wave function, it can be expected that the angular momentum does not depend on the particular path being enclosed. Furthermore, for global rotations, the current appears to be independent of the tilting angle of the ellipse. Thus, we conclude that, again, there is a sensitivity to the symmetries produced by the inhomogeneous gauge field in the elliptical ring trap (see discussion on the closed path integral in Appendix B).

V. SUMMARY AND CONCLUSIONS

We showed how a position-dependent artificial gauge field has a different impact on cold atomic gases in comparison to the case of homogeneous rotation [26,28–33]. In our sys-

tem, this difference between rotation and artificial gauge field appears as local rotations in addition to persistent currents (global rotation) simultaneously.

We investigated the behavior of the ground state of the BEC, which is trapped in a ring-shaped potential at the vicinity of a dielectric prism [38]. An artificial magnetic field is produced due to the interaction between the cold atomic gases and the evanescent field that emerges at the interface between the prism and vacuum area when the laser beam undergoes total internal reflection. As the system has sufficient degrees of freedom, we monitor the formation of invisible and visible vortices [28,44–48] by varying the strength of the gauge field. The position-dependent artificial magnetic field introduces a local angular momentum into the system, which results in the inhomogeneous formation of vortex structures in the BEC. This leads to the creation of vortices arranged in a single-line structure in the BEC which is aligned along the surface of the prism. The number and location of the vortices depend on the detuning, strength of the field, and the incident angle of the input laser beam.

Our study combines two phenomena: (i) a new kind of gauge fields, inhomogeneous artificial ones, that are currently under investigation experimentally in cold atom systems [49–51], producing inhomogeneous arrangements of vortices, and (ii) the superfluidity of BECs in toroidal traps, which have driven a lot of research in recent decades [18,19,23,56–58,62]. As such, our work can open new avenues to investigate the fundamental properties of vortices in 1D and 2D systems. For example, one can consider more complex artificial gauge field configurations, which as we have shown, can lead to peculiar combinations of local and global currents in the BEC. This in turn can also be used to detect or measure the actual position dependence of the artificial gauge field, by looking at the rotation or the vortices created in the bulk of the system. Another interesting approach would be to study the dynamics of this system and the interplay of visible and invisible vortices during time evolution. In particular, the nonlinear behavior of quantum systems that have rotation and vortices can lead to phenomena such as quantum turbulence [11,46,63]. The study of such effects in combination with our proposal, where vortices are formed in a linear structure, can lead to new dynamics.

APPENDIX A: HARMONIC TRAP

We plot the density of the ground state of the BEC which is trapped in a harmonic potential as well as the change in the angular momentum with respect to the artificial gauge field strength. We use the harmonic potential to show that the transition from the step to the linear regime that has been
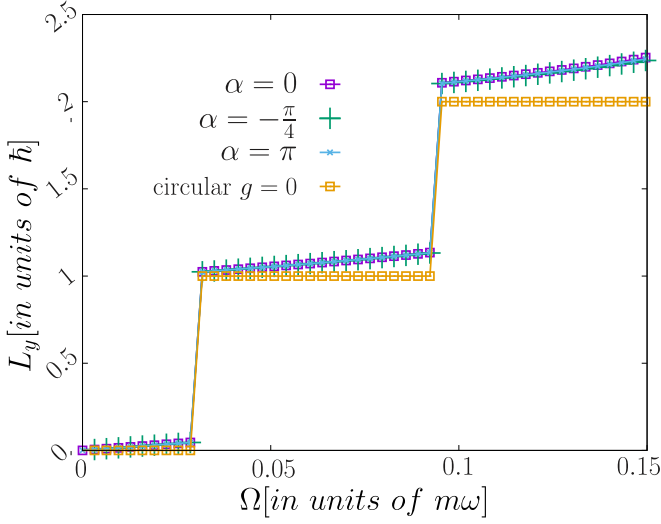
FIG. 9. Global current. Angular momentum L_y as a function of the induced rotation, Ω, for different values of the angle of the ellipse in a potential [see Eq. (4)]. Parameters of the 2D GPE are $g = 120$, $V_0 = 15$, and $a/b = \sqrt{1.5}$, $a = 25$, and length scale of $L = 30$. For the circular ring we choose a radius of $r \approx 5.36$. All parameters are given in harmonic oscillator units.

observed in Fig. 6 also occurs in the harmonic potential, and consequently, it is not a result of the shape of the potential. We observe a similar pattern of change in angular momentum as the amplitude of the gauge field, w_0, increases; at the beginning, the angular momentum of the system increases in steps and after a certain increase in the gauge field ($w_0 \approx 0.50$), it enters the linear regime. Furthermore, the healing length is $\xi_0 \approx 0.38$, and decreases as the strength of the gauge field increases.

The two distinguished regimes, i.e., quantized and linear, for the angular momentum resulting from the fact that the amount of angular moment added by one vortex depends not only on the number of vortices but also their size, as the size of the vortices is reduced as the strength of the gauge field increases. In other words, as the strength of angular momentum increases, the healing length reduces; consequently the amount of angular momentum that is added by one vortex to the BEC changes (see also Appendix C).

APPENDIX B: GLOBAL INDUCED ROTATION

In this section, we investigate the effects of a global rotation, Ω, on an elliptical ring trap potential. We compare these results with the ones obtained in the main text (see Fig. 7). In particular, we consider a GPE of the following form:

$$i\frac{\partial \phi}{\partial t} = \left[-\frac{1}{2}\nabla^2 + V_{\text{eff}}(x, z) + g|\phi|^2 - \Omega L_y \right]\phi. \quad (B1)$$

We note that, in Fig. 9, all the curves collapse; thus, there is no difference between the various angles of the ellipse. We also add a circular trap for comparison; however, this has a different radius, which produces a small displacement of the critical value that induces a current into the system. See [64]

TABLE I. Analytical calculation of the thickness of the BEC using the Thomas-Fermi approximation and a comparison with the threshold $16\sqrt{2}\xi_A$, also calculated analytically by including the field A in which vortices start to appear.

ω_0	v_0	δr	$16\sqrt{2}\xi_A$
0.60	0.25	7.78	6.76
0.65	0.35	6.95	6.36
0.70	0.50	6.17	5.98
0.75	0.70	5.52	5.64
0.90	0.85	5.17	5.30

for an example of the experimental realization of the plateaus of the current obtained in circular rings.

APPENDIX C: CONTINUITY EQUATION

From the Schrödinger equation one can obtain the continuity equation $\frac{\partial n}{\partial t} + \nabla \cdot j = 0$, with probability current of $j = n(x, z; t)\frac{\hbar}{m}\nabla S(r, t)$, where $n = \psi^*\psi$, is the density of the gas, and S is the phase of the wave function, $\psi(r, t) = \sqrt{n(r, t)}e^{iS(x, z; t)}$ [5]. For the inhomogeneous case, the equation that governs the system is obtained from a Gross-Pitaevskii equation and contains a term with an extra spatial dependence from the artificial gauge field [see Eq. (2)]. This leads us to the following equation:

$$\frac{\partial n}{\partial t} = \frac{i}{2}[\phi^*\nabla^2\phi - \phi\nabla^2\phi^*$$
$$+ 2i(\nabla \cdot \mathbf{A}|\phi|^2 + \phi^*\mathbf{A} \cdot \nabla\phi + \phi\mathbf{A} \cdot \nabla\phi^*)], \quad (C1)$$

where $j = \frac{i}{2}[\phi^*\nabla\phi - \phi\nabla\phi^* + 2i\phi^*A\phi]$.

In the absence of an inhomogeneous gauge field, by integration over the above equation, we obtain $\oint \nabla S \cdot dl = 2\pi q$, where q is an integer number. However, the presence of an inhomogeneous artificial gauge field ($A \neq 0$) would prevent us from easily writing Eq. (C1) in a compact form as $\nabla \cdot \mathbf{A} \neq 0$.
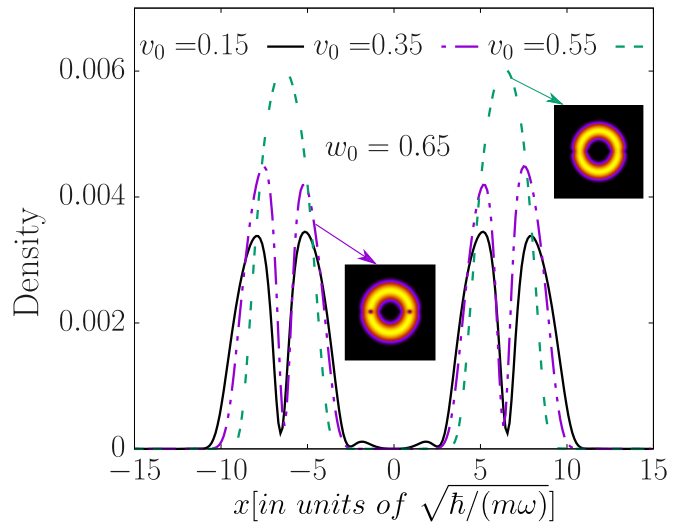

FIG. 10. Density for fixed ω_0. Density cuts of the full density displaying the vortices along the radial direction. Insets show two corresponding full density images. Parameters of the system are $g = 800$ and $w_0 = 0.65$, fixed for all curves.
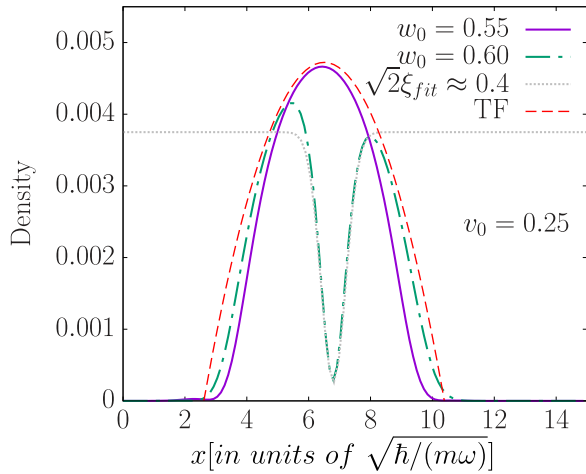
FIG. 11. Density for fixed v_0. Density cuts of the full density, displaying the transition from having no vortices to having vortices in the bulk. We compare the full density to the analytical Thomas-Fermi approximation. Parameters of the system are $g = 800$, and fixed $v_0 = 0.25$ with a potential given by $v_0(r - r_0)^2$ and $r_0 = 6.5$ for all curves. All parameters are given in harmonic oscillator units.

For our toy model,

$$\mathbf{\nabla} \cdot \mathbf{A} = -\frac{w_0}{\beta} \frac{1}{(1 + z^2/\beta^2)}. \quad \text{(C2)}$$

this would prevent us from presenting the integral from of probability current equation in a compact form. This equation can be used to explain why, in the elliptical case, the integral depends on the path for the inhomogeneous gauge field. It also indirectly explains how the position-dependent gauge field can affect the value of the angular momentum of a vortex added to the cold gas.

APPENDIX D: VORTICES INSIDE THE BEC BULK

In this section we briefly describe how the relation $\delta r \gtrsim 16\sqrt{2}\xi_A$ is found, with δr being the thickness of the BEC in the ring and ξ_A being the healing length.

We study the problem numerically and take $\sqrt{2}\xi_A$ as the typical vortex core length scale. However, note that this is not the true size of the vortex core, but only a length scale.
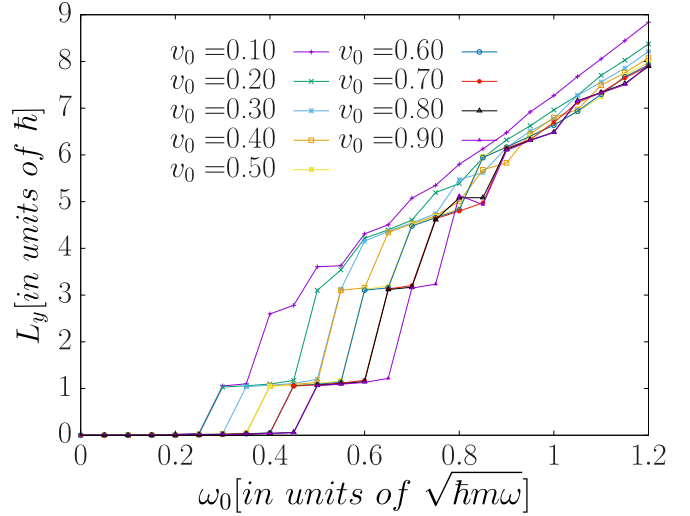

FIG. 12. Various trapping strengths. Angular momentum L_y vs the strength of the gauge field, w_0, for different values of the potential v_0. Parameters of the system are $g = 800$.

Therefore, we numerically calculate the prefactor at which vortices start to appear in the BEC bulk.

Using the Thomas-Fermi (TF) approximation, we find that for a trap of $v_0(r - r_0)^2$ and interactions g, the Thomas-Fermi radius reads $R_{\mathrm{TF}} - r0 = \pm 1/2(3/\pi)^{1/3}[g/(r_0 v_0)]^{2/6}$. Within the same approach, we also calculate the maximum density in the absence of w_0 to estimate the healing length. The results are presented in Table I. As we can see, these results give us a relatively good estimate for the appearance of vortices, but due to the symmetry of the system, small perturbations can lead to slight differences.

From Fig. 10 and Fig. 11 we can observe how the presence of a vortex inside the density bulk of the BEC creates a density minimum surrounded by two density maximums. This can be used to explain the reason why the prefactor is much larger than simply the vortex core size.

In Fiq. 12, we plotted the angular momentum, L_y, with respect to strength of gauge field, w_0, as the thickness of the ring changes v_0.

[1] W. Ketterle and N. V. Druten, Adv. At., Mol., Opt. Phys. **37**, 181 (1996).

[2] M. H. Anderson, J. R. Ensher, M. R. Matthews, C. E. Wieman, and E. A. Cornell, Science **269**, 198 (1995).

[3] M. D. Barrett, J. A. Sauer, and M. S. Chapman, Phys. Rev. Lett. **87**, 010404 (2001).

[4] W. D. Phillips, Rev. Mod. Phys. **70**, 721 (1998).

[5] C. J. Pethick and H. Smith, *Bose-Einstein Condensation in Dilute Gases* (Cambridge University Press, Cambridge, UK, 2008).

[6] I. Bloch, J. Dalibard, and W. Zwerger, Rev. Mod. Phys. **80**, 885 (2008).

[7] L. Pitaevskii and S. Stringari, *Bose-Einstein Condensation and Superfluidity* (Oxford University Press, New York, 2016), Vol. 164.

[8] A. Aftalion and Q. Du, Phys. Rev. A **64**, 063603 (2001).

[9] J.-Z. Wu, H.-Y. Ma, and M.-D. Zhou, *Vorticity and Vortex Dynamics* (Springer Science & Business Media, New York, 2007).

[10] P. G. Saffman, *Vortex Dynamics* (Cambridge University Press, Cambridge, UK, 1995).

[11] M. Tsubota, J. Phys. Soc. Jpn. **77**, 111006 (2008).

[12] M. Kobayashi and M. Tsubota, Phys. Rev. A **76**, 045603 (2007).

[13] M. C. Tsatsos, P. E. Tavares, A. Cidrim, A. R. Fritsch, M. A. Caracanhas, F. E. A. dos Santos, C. F. Barenghi, and V. S. Bagnato, Phys. Rep. **622**, 1 (2016).

[14] A. C. White, B. P. Anderson, and V. S. Bagnato, Proc. Natl. Acad. Sci. USA **111**, 4719 (2014).

[15] M. Paoletti and D. Lathrop, *Quantum Turbulence* (Annual Review of Condensed Matter Physics, 2011).

[16] K. Henderson, C. Ryu, C. MacCormick, and M. G. Boshier, New J. Phys. **11**, 043030 (2009).

[17] L. Amico, A. Osterloh, and F. Cataliotti, Phys. Rev. Lett. **95**, 063201 (2005).

[18] W. H. Heathcote, E. Nugent, B. T. Sheard, and C. J. Foot, New J. Phys. **10**, 043012 (2008).

[19] T. A. Bell, J. A. Glidden, L. Humbert, M. W. Bromley, S. A. Haine, M. J. Davis, T. W. Neely, M. A. Baker, and H. Rubinsztein-Duavezlop, New J. Phys. **18**, 035003 (2016).

[20] S. Gupta, K. W. Murch, K. L. Moore, T. P. Purdy, and D. M. Stamper-Kurn, Phys. Rev. Lett. **95**, 143201 (2005).

[21] A. S. Arnold, C. S. Garvie, and E. Riis, Phys. Rev. A **73**, 041606(R) (2006).

[22] L. Dobrek, M. Gajda, M. Lewenstein, K. Sengstock, G. Birkl, and W. Ertmer, Phys. Rev. A **60**, R3381 (1999).

[23] J. Polo, R. Dubessy, P. Pedri, H. Perrin, and A. Minguzzi, Phys. Rev. Lett. **123**, 195301 (2019).

[24] F. Piazza, L. A. Collins, and A. Smerzi, Phys. Rev. A **80**, 021601(R) (2009).

[25] A. C. Mathey and L. Mathey, New J. Phys. **18**, 055016 (2016).

[26] K. W. Madison, F. Chevy, W. Wohlleben, and J. Dalibard, Phys. Rev. Lett. **84**, 806 (2000).

[27] D. L. Feder, C. W. Clark, and B. I. Schneider, Phys. Rev. A **61**, 011601(R) (1999).

[28] M. Tsubota, K. Kasamatsu, and M. Ueda, Phys. Rev. A **65**, 023603 (2002).

[29] A. L. Fetter, Rev. Mod. Phys. **81**, 647 (2009).

[30] K. W. Madison, F. Chevy, V. Bretin, and J. Dalibard, Phys. Rev. Lett. **86**, 4443 (2001).

[31] M. R. Matthews, B. P. Anderson, P. C. Haljan, D. S. Hall, C. E. Wieman, and E. A. Cornell, Phys. Rev. Lett. **83**, 2498 (1999).

[32] J. R. Abo-Shaeer, C. Raman, J. M. Vogels, and W. Ketterle, Science **292**, 476 (2001).

[33] P. Engels, I. Coddington, P. C. Haljan, and E. A. Cornell, Phys. Rev. Lett. **89**, 100403 (2002).

[34] E. Hodby, G. Hechenblaikner, S. A. Hopkins, O. M. Maragò, and C. J. Foot, Phys. Rev. Lett. **88**, 010405 (2001).

[35] J. E. Williams, E. Zaremba, B. Jackson, T. Nikuni, and A. Griffin, Phys. Rev. Lett. **88**, 070401 (2002).

[36] J. E. Williams and M. J. Holland, Nature (London) **401**, 568 (1999).

[37] R. M. Price, D. Trypogeorgos, D. L. Campbell, A. Putra, A. Valdés-Curiel, and I. B. Spielman, New J. Phys. **18**, 113009 (2016).

[38] M. Mochol and K. Sacha, Sci. Rep. **5**, 7672 (2015).

[39] R. Sachdeva and T. Busch, Phys. Rev. A **95**, 033615 (2017).

[40] V. E. Lembessis, A. Alqarni, S. Alshamari, A. Siddig, and O. M. Aldossary, J. Opt. Soc. Am. B **34**, 1122 (2017).

[41] S. McEndoo and T. Busch, Phys. Rev. A **79**, 053616 (2009).

[42] N. Lo Gullo, T. Busch, and M. Paternostro, Phys. Rev. A **83**, 053612 (2011).

[43] L. Wen and X. Luo, Laser Phys. Lett. **9**, 618 (2012).

[44] K. Kasamatsu, M. Tsubota, and M. Ueda, Phys. Rev. Lett. **91**, 150406 (2003).

[45] K. Kasamatsu and K. Sakashita, Phys. Rev. A **97**, 053622 (2018).

[46] K. Kasamatsu, M. Tsubota, and M. Ueda, Phys. Rev. A **67**, 033610 (2003).

[47] L. Wen, H. Xiong, and B. Wu, Phys. Rev. A **82**, 053627 (2010).

[48] L. Wen, Y. Qiao, Y. Xu, and L. Mao, Phys. Rev. A **87**, 033604 (2013).

[49] N. Goldman, G. Juzeliūnas, P. Öhberg, and I. B. Spielman, Rep. Prog. Phys. **77**, 126401 (2014).

[50] V. Galitski, G. Juzeliūnas, and I. B. Spielman, Phys. Today **72**(1), 38 (2019).

[51] M. Aidelsburger, *Artificial Gauge Fields with Ultracold Atoms in Optical Lattices* (Springer, New York, 2015).

[52] S. S. S. Hejazi, J. Polo, R. Sachdeva, and T. Busch, Phys. Rev. A **102**, 053309 (2020).

[53] A. A. Abrikosov, Sov. Phys. JETP **5**, 1174 (1957).

[54] A. S. Bradley, C. W. Gardiner, and M. J. Davis, Phys. Rev. A **77**, 033616 (2008).

[55] L. J. O'Riordan, A. C. White, and T. Busch, Phys. Rev. A **93**, 023609 (2016).

[56] T. Bland, Q. Marolleau, P. Comaron, B. Malomed, and N. Proukakis, J. Phys. B: At., Mol. Opt. Phys. **53**, 115301 (2020).

[57] M. de Goër de Herve, Y. Guo, C. D. Rossi, A. Kumar, T. Badr, R. Dubessy, L. Longchambon, and H. Perrin, J. Phys. B: At., Mol. Opt. Phys. **54**, 125302 (2021).

[58] P. Navez, S. Pandey, H. Mas, K. Poulios, T. Fernholz, and W. Von Klitzing, New J. Phys. **18**, 075014 (2016).

[59] W. Bao, D. Jaksch, and P. A. Markowich, J. Comput. Phys. **187**, 318 (2003).

[60] For a uniform BEC, the size of the core of the vortex is the order of the healing length $\xi = (8\pi n a_m)^{-1/2}$, where n is the density of the system and a_m is twice of atomic scattering length, $a_m = 2a$ [65]. Also the ratio between ξ and the radius r of the condensate takes the form of $\xi/R = (a_{ho}/R)^2$ [66].

[61] U. Eckern and P. Schwab, J. Low Temp. Phys. **126**, 1291 (2002).

[62] J. M. Gomez Llorente and J. Plata, Phys. Rev. A **100**, 043613 (2019).

[63] W. Vinen and J. Niemela, J. Low Temp. Phys. **128**, 167 (2002).

[64] K. C. Wright, R. B. Blakestad, C. J. Lobb, W. D. Phillips, and G. K. Campbell, Phys. Rev. Lett. **110**, 025302 (2013).

[65] J. Tempere, M. Wouters, and J. T. Devreese, Phys. Rev. A **71**, 033631 (2005).

[66] G. Baym and C. J. Pethick, Phys. Rev. Lett. **76**, 6 (1996).